Imaging retinal structures at cellular-level resolution by visible-light optical coherence tomography

Shaohua Pi, Tristan T. Hormel, Xiang Wei, William Cepurna, John C. Morrison, and Yali Jia*

Casey Eye Institute, Oregon Health & Science University, Portland, Oregon 97239, USA
Corresponding author: jiaya@ohsu.edu

In vivo high-resolution images are the most direct way to understand retinal function and diseases. Here we report the use of visible-light optical coherence tomography with volumetric registration and averaging to achieve cellular-level retinal structural imaging in a rat eye, covering the entire depth of the retina. Vitreous fibers, nerve fiber bundles, and vasculature were clearly revealed, as well as at least three laminar sublayers in the inner plexiform layer. We also successfully visualized ganglion cell somas in the ganglion cell layer, cells in the inner nuclear layer, and photoreceptors in the outer nuclear layer and ellipsoid zone. This technique provides, to the best of our knowledge, a new means to visualize the retina *in vivo* at a cellular resolution and may enable detection or discovery of cellular neuronal biomarkers to help better diagnose ocular disease.   © 2020 Optical Society of America

https://doi.org/10.1364/OL.386454

The retina consists of numerous types of neurons, such as photoreceptor cells, bipolar cells, and ganglion cells, as well as various supporting cells and tissues for visual function [1]. Although histological methods can reveal these cells at a very fine level of detail, visualizing them *in vivo* is still highly desirable. Improving methods of evaluating longitudinal progression of retinal damage in ocular diseases at the cellular level and biomarkers from individual neuronal cells will be helpful both scientifically and clinically.

Visible-light optical coherence tomography (vis-OCT) [2] is an emerging imaging modality that can achieve higher axial resolution than standard OCT, which relies on infrared light sources [3]. We have established a fiber-based prototype vis-OCT, which covers the visible-light band with a super-continuum laser from 510 to 610 nm. The system is calibrated to 1.2 µm axial resolution in tissue, 6 µm lateral resolution, 1.8 mm imaging depth, and 89 dB sensitivity in air with a protective silver mirror and USAF-1951 target at an illumination of 0.8 mW light power and 0.58 mm Gaussian beam at the cornea [4]. Using this vis-OCT, we have previously demonstrated high-resolution angiographic and structural retinal imaging in the rat [4]. However, the image quality is still limited by speckle noise. To address this issue, speckle reduction using scan modulation was recently explored in a vis-OCT system and achieved up to a 2.35 dB improvement in contrast-to-noise ratio in speckle-reduced images [5]. In this Letter, by effectively reducing speckle noise through registering multiple volumes [6,7] prior to retinal layer segmentation, we imaged neurons in the rat retina, taking full advantage of the high-axial-resolution of vis-OCT. This multi-volume registration allowed us to achieve cellular-resolution images over entire depth of the retina.

In this Letter, retinal images of a Brown Norway rat (20-weeks-old, male, ~300 grams, N = 1) were acquired using a previously described protocol [8]. The animal was anesthetized with inhaled 2.5% isoflurane during imaging. Volumetric raster scans were collected from the inferior retina within a $10 \times 10°$ field of view (Fig. 1A), approximately 1.5 mm from the optic disc. The field of view was approximately 1×1 mm^2, considering the 6 mm axial length of the rat eye. We used an imaging protocol that could generate OCT and OCT angiography (OCTA) images simultaneously. Each volume had 512 A-lines for each B-scan, two repeated B-scans at each slow scan position, and 512 slow scan positions. In each imaging session, five volumes were recorded, with eyes moisturized in a 10 s interval between sessions. With a sampling rate of 50 kHz, a full session took about 1 min to complete. A total of 22 imaging sessions were performed, taking approximately a half-hour, resulting in 110 volumes for registration [6] and averaging to suppress the speckle noise. (Progressive image contrast improvement is shown in Visualization 1, Visualization 2 and Visualization 3). Temporary photoreceptor bleaching might occur in the rat during imaging due to visible-light exposure. All experimental procedures were approved by the Institutional Review Board/Ethics Committee, as well as the Institutional Animal Care and Use Committee (IACUC) of Oregon Health & Science University (OHSU).

The recorded interferogram was processed by previously described procedures to obtain structural and angiographic
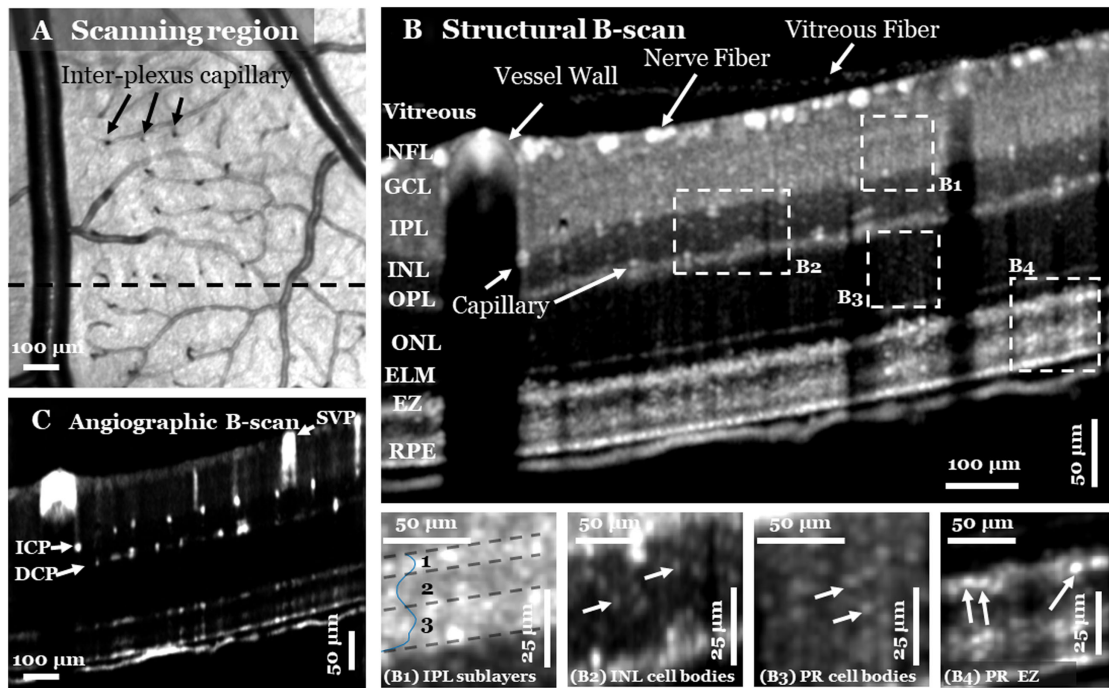
Fig. 1. (A) Mean *en face* projection structural vis-OCT of a rat retina with $1 \times 1-mm^2$ field of view from an averaged volume scan (N = 110). Inter-plexus capillaries (arrows) can be recognized as dark dots. The black dashed line indicates the location of the B-scan shown in (B) and (C). (B) Structural B-scan from the averaged volume visualizes (B1) at least three sub-laminar layers in the IPL, (B2) INL cell bodies, photoreceptor (PR) (B3) cell bodies, and (B4) EZ. The blue curve in (B1) is the averaged structural depth profile of the IPL. The white arrows indicate the representative neuronal cells. (C) Corresponding angiographic B-scan demonstrates large vessels and single capillaries. The flow signals in the outer retina are due to projection artifacts. SVP, superficial vascular plexus; ICP, intermediate capillary plexus; DCP, deep capillary plexus.

OCT volumes [4]. Unlike previous 3-D volume registration techniques [6], we treated the lateral and axial directions heterogeneously to achieve fast and robust registration. Such heterogeneous registration is appropriate in this context, since changes in illumination are almost negligible along the depth during multiple volume scans, and non-rigid deformation occurs mainly in the lateral, rather than axial, direction. In the lateral direction, non-rigid registration using B-spline, free-form deformation [9] was performed on *en face* images, which were generated by maximum projection of the OCTA signal along the entire A-lines. The transformation coefficients obtained from *en face* images were then applied to all depth planes in the volumes. In the axial direction, the reconstructed A-lines at each lateral position were axially aligned using cross correlation. All registered volumes were then merged and averaged, resulting in the averaged structural and angiographic volumes used for further analysis. It should be noted that prior layer segmentation was not necessary for the volume registration we proposed here. All enhancement processes mentioned below were performed by manually identifying the cells and then forming binary images which were subsequently Gaussian-filtered. All images shown in linear scale in this Letter are from one registered and merged scan from a single animal.

Figure 1A is a mean *en face* structural vis-OCT of a rat retina from the averaged structural volume, while Figs. 1B and 1C show corresponding structural and angiographic B-scans, respectively. Retinal layers in 1B can be clearly differentiated by reflectance contrast. The nerve fiber bundles appear brightest. They are sparse and are separated by gaps in this region (1.5 mm

from the optic disc). At least three laminar sublayers within the inner plexiform layer (IPL) can be confirmed with a bright-dark-bright transition pattern (Fig. 1B1). If accounting for more possible sublayers in IPL-3, the findings are similar to those that have recently been observed in the human retina with vis-OCT [10]. The inner nuclear layer (INL) cells (Fig. 1B2) and photoreceptor cell bodies (Fig. 1B3) in the outer nuclear layer (ONL) and ellipsoid zone (EZ) (Fig. 1B4) can also be identified. These structures are better appreciated in the B-scan fly-through video (Visualization 4) and correspond to a published human retinal image taken near the fovea using a histological immuno-histochemistry method [11]. The walls of major retinal vessels (diameter ≈ 100 μm) can also be successfully identified on
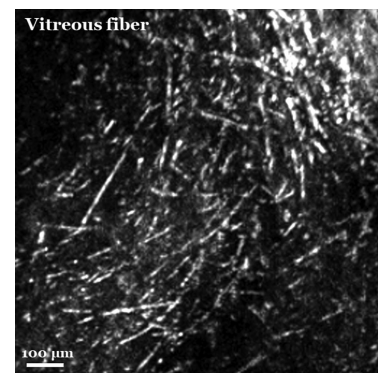

Fig. 2. *En face* maximum projection of reflectance signal in the posterior vitreous. The vitreous fibers interdigitate with each other.

OCT structural images in the retina (Fig. 1B). Cross sections of individual capillaries in the intermediate and deep plexuses are discernible in structural B-scans (Fig. 1B) at the inner and outer boundary of the INL, respectively, and are clearly distinguishable from the surrounding tissues in the angiographic B-scan (Fig. 1C, Visualization 5).

By projecting the slab anterior to the inner limiting membrane, randomly oriented posterior vitreous fibers were revealed _in vivo_ for the first time, to the best of our knowledge (Fig. 2). Their morphological appearance was similar to that visualized in a post-mortem human eye by transmission electron microscopy (TEM) [12]. The appearance of the nerve fiber bundles can be appreciated in the _en face_ image (Fig. 3A), which presents a much larger field of view than that achieved with adaptive optics (AO) OCT [13]. The nerve fibers in the rat retina are supplied anteriorly by the microvasculature of the superficial vascular plexus (SVP) (Fig. 3A). Near the disc, tightly associated fibers form bundles that appear thicker in the cross section (Figs. 3A1 and 3A2). As the distance from the optic disc increases, the bundles spread out along the surface of the ganglion cell layer, leading to a relatively constant nerve fiber area density (percentage of occupied area to total area, excluding the vasculature) of ~47% across the field of view. Ganglion cell somas (Fig. 3B) were observed by maximum projection of the slab just beneath the nerve fiber slab. To calculate the soma diameter, the binary image of somas (Fig. 3B1) was manually delineated in up-sampled (factor = 4) images. Then a watershed transform [14] was applied to separate overlapping somas (Fig. 3B2), resulting in a total of N = 290 identified cell somas. A histogram of soma diameter (Fig. 3B3) roughly obeys a normal distribution with a 15.4 µm mean value and a 6.0 µm standard deviation, which is consistent with a previously reported value of 16.3 µm by confocal microscopy in the rat [15]. INL cell bodies, including bipolar cell, amacrine cells and other cells, could also be visualized in the _en face_ image of the INL slab using maximum projection (Fig. 3C). In a 0.43×0.43 mm region of interest, 206 contrast-enhanced cells were counted, resulting in a density of approximately ~1100 cells/mm^2. Certainly, this density may be an underestimate [16] due to the limited transverse resolution of this technique.

With the high contrast angiogram, three vascular plexuses could be clearly observed. The retinal circulatory organization could be illustrated by overlaying the three vascular plexuses (Fig. 4A). By further overlaying the plexuses with the NFL (Fig. 4B), the nourishment of vessel to nerve fibers was observed by inter-plexus capillaries (white dots, manually identified). Capillaries in the intermediate and deep capillary plexuses could be identified in the _en face_ structural OCT, since capillaries had stronger reflectance than the surrounding tissue (Figs. 4C and 4D). These vascular networks resolved by structural vis-OCT corresponded well to their _en face_ OCT angiograms (Figs. 4E and 4F), although the contrast was lower.

The performance of vis-OCT was also demonstrated by the ability to focus on both the inner and outer retina simultaneously. Photoreceptor cell bodies (Fig. 4G) and EZ (Fig. 4H) were revealed by maximum projection of the ONL slab and EZ slab, although cellular structures were affected by vessel shadows. In the overlay images (Figs. 4I and 4J), photoreceptor cell bodies and the EZ are found to be evenly distributed in the normal retina.
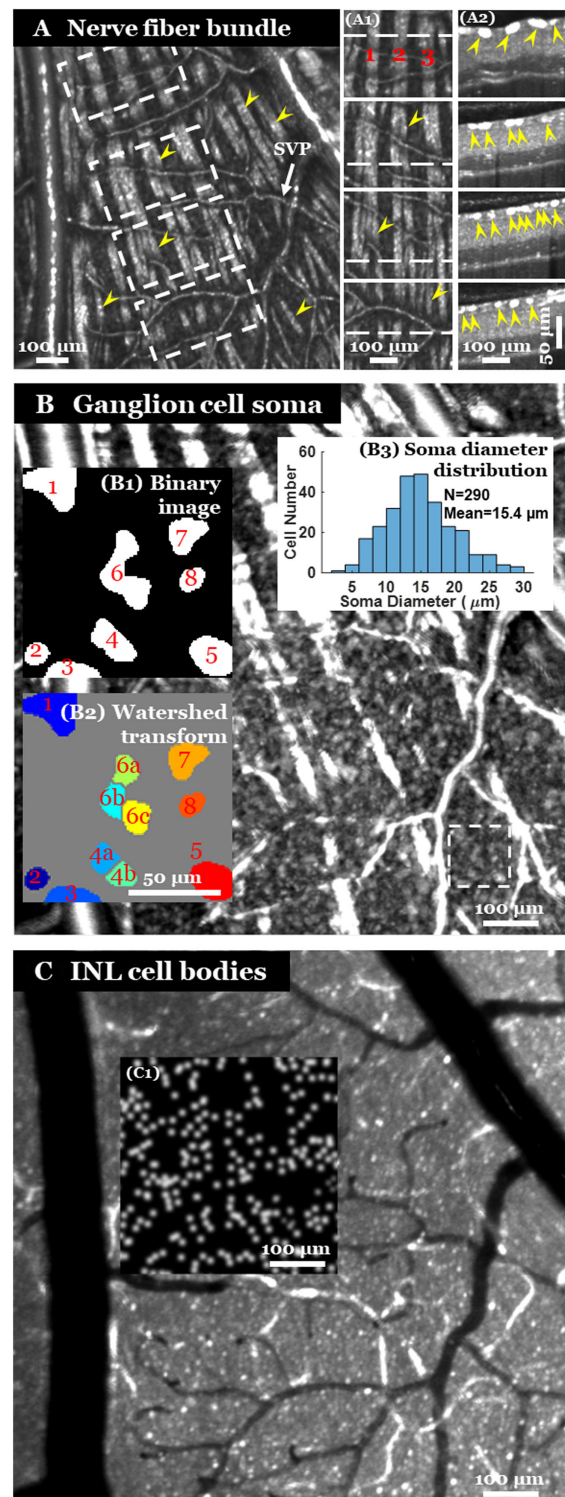

Fig. 3. _En face_ images on specific slabs demonstrate (A), nerve fiber bundles (arrowhead); (B) ganglion cell somas; and (C) INL cells bodies.

Currently, _in vivo_ visualization of cellular structures in the retina requires AO [6,17]. The images acquired by vis-OCT are comparable in their ability to visualize nerve fiber bundles, but less effective in resolving photoreceptor cells compared to infrared AO-OCT. However, using a smaller numerical
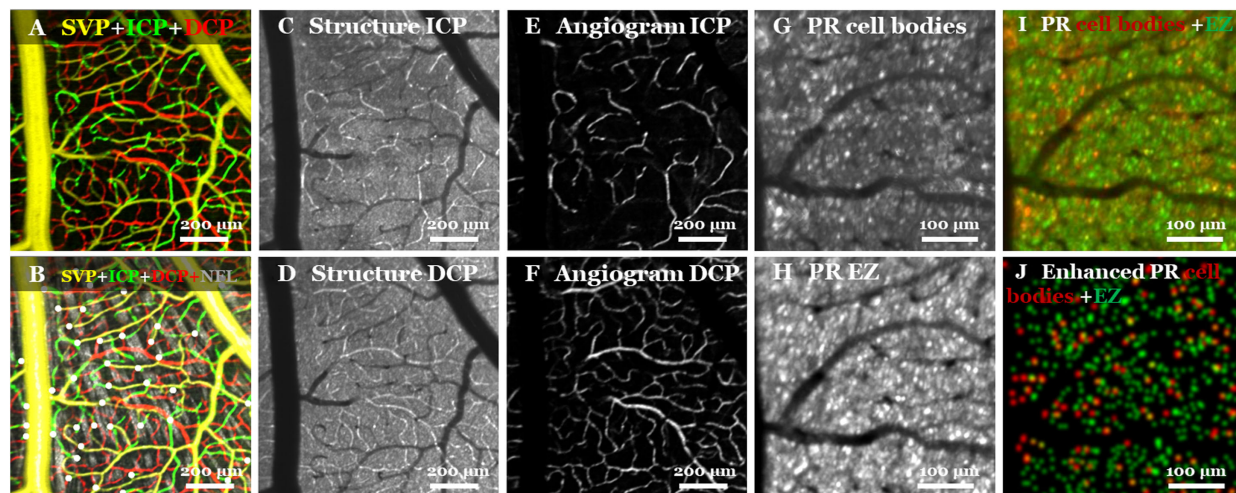
Fig. 4. (A)–(F) *En face* projections of the rat retinal microcirculation showing the appearance (A) without and (B) with structural NFL; (C) structural ICP; (D) DCP; (E) angiographic ICP; and (F) DCP. Inter-plexus capillaries are marked as white dots in (B). (G)–(J) Enlarged *en face* view of photoreceptor cell bodies in the (G), ONL slab and (H), EZ, as well as their appearance in (I), the original and (J), the manually enhanced overlay.

aperture, vis-OCT can cover the entire depth of the retina and resolve more types of cells than infrared AO-OCT. In addition, compared to the work most recently reported by Zhang *et al.* [7], which uses volumetric averaging while operating in infrared light, our vis-OCT demonstrated more detailed cellular visualization, particularly for nerve fiber bundles, photoreceptor cell bodies, and additional INL cell bodies. A long acquisition time currently limits clinical application of this technique, although human retinal images have been obtained by vis-OCT [10,18]. In the future, integration of AO with vis-OCT could minimize acquisition time by enabling a higher sampling rate and reducing the number of required volumes to achieve cellular resolution. While cell types in healthy eyes can be confidently determined based on location and morphology, tissue and cell component alterations in clinically diseased eyes may make these distinctions more difficult. Type-specific imaging will require more advanced techniques in order to correctly differentiate cell types and explore potentially valuable biomarkers. Possible ways of accomplishing this may include the assistance of spectroscopic contrast [19].

In summary, with the aid of multiple volume registration, we have achieved cellular-resolution imaging in the rat retina using vis-OCT. This allowed us to quantify the number, size, and density of neuronal cells and compare their appearance with that achieved by other imaging methods. We believe this represents a promising advance in noninvasive retinal imaging.

REFERENCES

1. A. P. Schachat, C. P. Wilkinson, D. R. Hinton, P. Wiedemann, K. B. Freund, and D. Sarraf, *Ryan's Retina* (Elsevier Health Sciences, 2017).
2. X. Shu, L. J. Beckmann, and H. F. Zhang, J. Biomed. Opt. **22**, 121707 (2017).
3. W. Drexler and J. G. Fujimoto, *Optical Coherence Tomography: Technology and Applications* (Springer, 2008).
4. S. Pi, A. Camino, M. Zhang, W. Cepurna, G. Liu, D. Huang, J. Morrison, and Y. Jia, Biomed. Opt. Express **8**, 4595 (2017).
5. I. Rubinoff, L. Beckmann, Y. Wang, A. A. Fawzi, X. Liu, J. Tauber, K. Jones, H. Ishikawa, J. S. Schuman, and R. Kuranov, Neurophotonics **6**, 041107 (2019).
6. Z. Liu, K. Kurokawa, F. Zhang, J. J. Lee, and D. T. Miller, Proc. Natl. Acad. Sci. USA **114**, 12803 (2017).
7. P. Zhang, E. B. Miller, S. K. Manna, R. K. Meleppat, E. N. Pugh, and R. J. Zawadzki, Neurophotonics **6**, 041105 (2019).
8. S. Pi, T. T. Hormel, X. Wei, W. Cepurna, A. Camino, Y. Guo, D. Huang, J. C. Morrison, and Y. J. N. Jia, Neurophotonics **6**, 041104 (2019).
9. D. Rueckert, L. I. Sonoda, C. Hayes, D. L. Hill, M. O. Leach, and D. J. Hawkes, IEEE Trans. Med. Imaging **18**, 712 (1999).
10. T. Zhang, A. M. Kho, and V. J. Srinivasan, Biomed. Opt. Express **10**, 2918 (2019).
11. N. Cuenca, I. Ortuño-Lizarán, and I. Pinilla, Ophthalmology **125**, 407 (2018).
12. J. Sebag and E. Balazs, Invest. Ophthalmol. Visual Sci. **30**, 1867 (1989).
13. Y. Jian, J. Xu, M. A. Gradowski, S. Bonora, R. J. Zawadzki, and M. V. Sarunic, Biomed. Opt. Express **5**, 547 (2014).
14. F. Meyer, Signal Process. **38**, 113 (1994).
15. S. Hattar, H.-W. Liao, M. Takao, D. M. Berson, and K.-W. Yau, Science **295**, 1065 (2002).
16. E. Strettoi, E. Novelli, F. Mazzoni, I. Barone, and D. Damiani, Prog. Retinal Eye Res. **29**, 272 (2010).
17. M. Pircher and R. J. Zawadzki, Biomed. Opt. Express **8**, 2536 (2017).
18. J. Yi, S. Chen, X. Shu, A. A. Fawzi, and H. F. Zhang, Biomed. Opt. Express **6**, 3701 (2015).
19. R. Qian, W.-F. Huang, R. P. McNabb, K. C. Zhou, Q. H. Liu, A. N. Kuo, and J. A. Izatt, Biomed. Opt. Express **10**, 3281 (2019).